

# Interplay between deformation behavior and mechanical properties of intercritically annealed and tempered medium-manganese transformation-induced plasticity steel



Z.H. Cai <sup>a,\*</sup>, H. Ding <sup>a</sup>, H. Kamoutsi <sup>b</sup>, G.N. Haidemenopoulos <sup>b</sup>, R.D.K. Misra <sup>c,\*</sup>

<sup>a</sup> School of Materials and Metallurgy, Northeastern University, Shenyang 110819, China

<sup>b</sup> Department of Mechanical Engineering, University of Thessaly, Volos, Greece

<sup>c</sup> Department of Metallurgical and Materials Engineering, University of Texas at El Paso, El Paso, TX 79968, USA

## ARTICLE INFO

### Article history:

Received 1 December 2015

Received in revised form

12 December 2015

Accepted 14 December 2015

Available online 19 December 2015

### Keywords:

TRIP steels

Austenite stability

Mechanical properties

Work hardening

Simulations

## ABSTRACT

We elucidate the mechanistic contribution of the interplay between microstructural constituents and plastic deformation behavior of a hot rolled Fe–0.18C–10.62Mn–4.06Al–0.03Nb transformation-induced plasticity (TRIP) steel that was characterized by excellent tensile elongation (TE) of 48%, ultimate tensile strength (UTS) of 1012 MPa, and yield ratio of 0.58. The excellent mechanical properties were a cumulative contribution of TRIP effect, discontinuous TRIP effect, and the cooperative deformation of austenite,  $\delta$ -ferrite, and  $\alpha$ -ferrite, such that the austenite stability dictated the ultimate mechanical properties and the dynamic composite nature of the three stages of work hardening. More importantly, the austenite stability was governed by the combination of intercritical annealing and tempering treatment, when partitioning of carbon and manganese took place; an aspect supported by the simulation of intercritical annealing condition via DICTRA. The study underscores the significance of intercritical annealing in conjunction with tempering as a viable route to obtain the desired mechanical properties in the new generation of advanced high strength steels (TRIP steels).

© 2015 Elsevier B.V. All rights reserved.

## 1. Introduction

It is well known that austenite plays a significant role in obtaining excellent combination of strength and ductility in transformation-induced plasticity (TRIP) steels. The microstructure of conventional TRIP steels consists of ferrite as the dominant phase (55–65%), retained austenite (< 20%), bainite (25–35%), and occasionally a small amount of martensite [1–3]. Recent studies [4–8] focused on medium-Mn (5–12%) TRIP steels suggested that superior mechanical properties can be obtained with increase in Mn- and C-content, which increases the volume fraction of retained austenite (20–80%).

An innovative heat treatment, referred as “austenite reversed transformation” (ART), was applied to medium-Mn steels [4–7,9–11]. Retained austenite was obtained by successive enrichment of Mn and C in the reversed austenite during the intercritical process. However, ART-annealing was not applicable to the experimental steel, and quenching and tempering (Q&T) was envisioned by us as an alternative and effective heat treatment [12,13]. Tempering is

often used to relieve the residual stress. However, it generally leads to the decomposition of retained austenite into ferrite and cementite, which is detrimental to ductility. It was reported that [14,15] the amount of retained austenite was decreased with increase in tempering temperature in steels containing 2 wt% Mn. A large fraction of austenite continued to remain in Fe–0.2C–5Mn (wt%) steel after tempering at 400 °C [16]. The decomposition temperature of austenite increased with increasing Mn content [17], which suggested that the thermal stability of austenite can be enhanced by the enrichment of Mn. Thus, it is possible for austenite in the medium-Mn steels to remain stable during the tempering process. Moreover, it was observed that the precipitation of carbides during tempering led to decrease in the austenite fraction. Thus, Al was added to medium-Mn steels, where the role of Al was to optimize austenite stability by suppressing cementite formation [18].

Austenite stability against mechanically-induced transformation to martensite is known to depend on chemical composition, austenite size, austenite morphology and stress state [12,19].  $M_s$  is the athermal martensite start temperature. The stability of retained austenite can be characterized by  $M_s^g$  temperature, at which the stress required to trigger stress-assisted transformation attains the yield strength [20]. In the  $M_s \sim M_s^g$  temperature range, martensite nucleation on existing nucleation sites is enhanced by

\* Corresponding authors.

E-mail addresses: [tsaizhihui@163.com](mailto:tsaizhihui@163.com) (Z.H. Cai), [dmsira2@utep.edu](mailto:dmsira2@utep.edu) (R.D.K. Misra).

stress, i.e. stress-assisted transformation of austenite to martensite takes place. In the  $M_s \sim M_d$  temperature range, martensite formation occurs on nucleation sites introduced by plastic deformation, such as slip band intersections, where strain induced transformation of austenite to martensite occurs. No transformation takes place at temperatures higher than the  $M_d$  temperature. Therefore, austenite stability is influenced by the deformation temperature, and accounts for the different martensite transformation mechanisms (stress-assisted or strain-induced).

From the above discussion, tempering had a significant impact on retained austenite content and stability. To study the effect of mechanism of martensite transformation on mechanical properties, samples with different austenite stability were obtained by tempering at different temperature. The objective of the study is to elucidate the tempering effects on the mechanical properties and deformation behavior of a hot-rolled medium manganese steel.

## 2. Experimental

The chemical composition of the experimental TRIP steel had a nominal composition of Fe-0.18C-0.62Mn-4.06Al-0.03Nb (wt%). The selected composition is based on the role of alloying elements and an equilibrium thermodynamic analysis that is discussed elsewhere [12]. A 40 kg experimental steel ingot was cast after melting the steel in a vacuum induction furnace. The ingot was heated at 1200 °C for 2 h, hot forged into rods of section size 100 mm × 30 mm, then air-cooled to room temperature. Subsequently, the rods were soaked at 1250 °C for 2 h, hot-rolled to 4 mm thick strip, and finally air cooled to room temperature.

In order to establish appropriate heat treatment schedule, the critical temperatures of  $A_{c1}$  and  $A_{c3}$  of the experimental steel obtained by dilatometry were 585 °C and 820 °C, respectively. The as-hot-rolled sheets were subjected to quenching and tempering (Q&T) heat treatment for reasons discussed in the introduction section. First, they were soaked in a high temperature furnace at 775 °C for 1 h, and then immediately quenched in water. Second,

the quenched samples were tempered at 300 °C, 400 °C, 500 °C, 600 °C for 1 h, respectively, followed by air cooling.

Specimens of 12.5 mm width and gage length of 50 mm were subjected to tensile tests using a universal testing machine (SANSMT 5000) at a constant crosshead speed of 3 mm min<sup>-1</sup> at room temperature. Prior to the tensile tests, the uneven surface of the samples was polished. The samples were etched with 25% sodium bisulfite aqueous solution. Microstructural examination was carried out using scanning electron microscope (SEM), electron microprobe analysis (EMPA) and transmission electron microscope (TEM). Austenite volume fraction was determined by X-ray diffraction (XRD) based on the integrated intensities of  $(200)_\alpha$ ,  $(211)_\alpha$ ,  $(200)_\gamma$ ,  $(220)_\gamma$  and  $(311)_\gamma$  diffraction peaks [21].

The austenite formation and associated solute partitioning during intercritical annealing and tempering were simulated with DICTRA software [22] using the TCFE6 thermodynamic database and the MOBFE2 mobility database for ferrous alloys.

## 3. Results and discussion

### 3.1. Microstructure

The SEM micrograph of as-hot-rolled sample quenched from 775 °C is presented in Fig. 1a. Fig. 1b–e describe the microstructure of the quenched samples that were tempered in the temperature range of 300–600 °C. The microstructural constituents comprised of austenite, layered  $\delta$ -ferrite, and acicular  $\alpha$ -ferrite that formed during intercritical annealing. For clarity, the magnified region of ferrite, marked with rectangle in Fig. 1e, is presented in Fig. 1f. The two kinds of ferrite differed in morphology, but also in micro-hardness (Table 1).

The variation in the volume fraction of austenite obtained from XRD is summarized in Fig. 2c. The austenite content in the untempered sample and samples tempered in the range of 300–500 °C was essentially similar, except for a small decrease in the sample tempered at 600 °C. Based on the SEM micrographs and

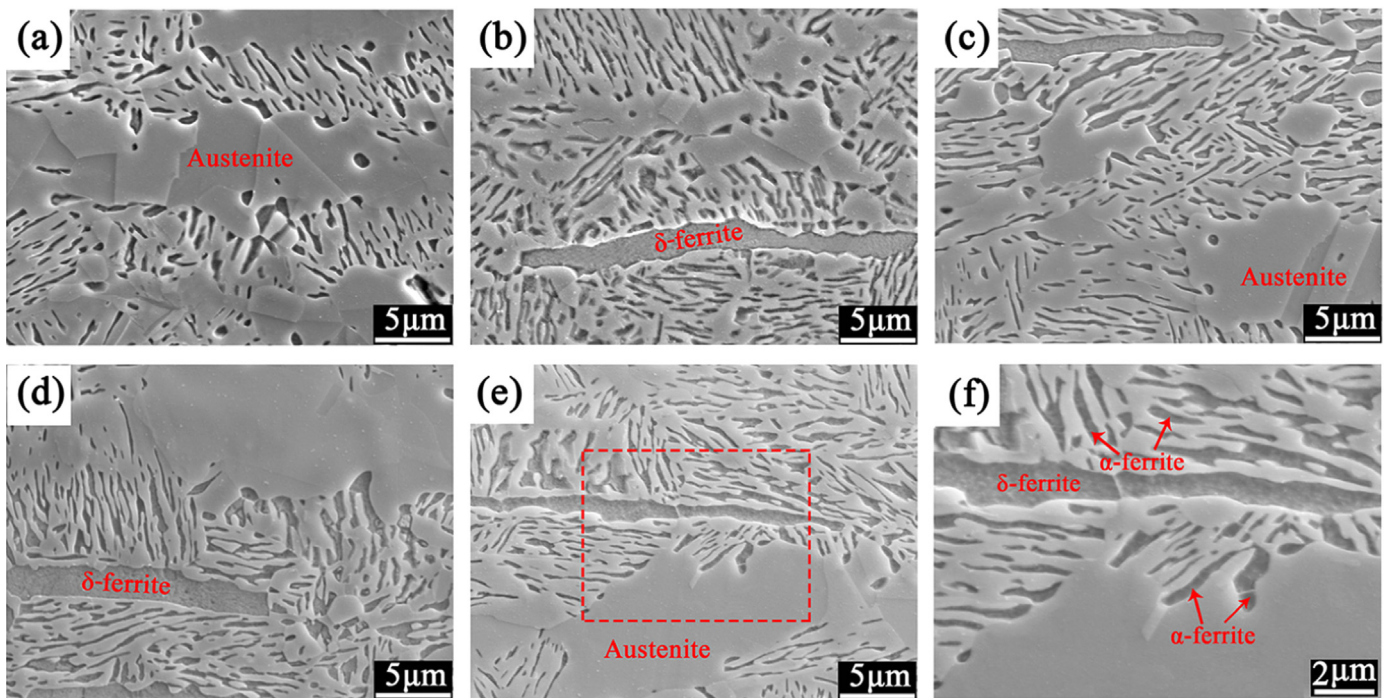


Fig. 1. SEM micrographs of samples quenched from 775 °C and then tempered at different temperatures. (a) Untempered, (b) 300 °C, (c) 400 °C, (d) 500 °C, (e) 600 °C, and (f) higher magnification of the boxed region in (e).

**Table 1**  
Microhardness of constituent phases.

Phases	Vickers hardness (HV)
$\delta$ -ferrite	252 $\pm$ 6
$\alpha$ -ferrite	302 $\pm$ 15
Austenite	233 $\pm$ 10
Martensite	450 $\pm$ 10

XRD results, the microstructural difference between the untempered sample and the tempered samples was not significant, but the corresponding mechanical properties varied in a systematic manner.

### 3.2. Mechanical properties

Fig. 3 demonstrates excellent combinations of TE of 40–55%, UTS of 860–1150 MPa, yield ratio of 0.45–0.72, and UTS  $\times$  TE of 42–49 GPa%, which are superior to the values reported for hot-rolled medium-Mn TRIP steels. The ultimate tensile strength (UTS) decreased continuously with increase in tempering temperature, whereas yield strength (YS) and total elongation (TE) increased with increase in tempering temperature. The decrease in UTS as a function of tempering temperature was estimated using Eq. (1). Eq. (1) has been proven to provide an estimate of the tensile flow stress of multiphase TRIP steels [5,23–26]:

$$\sigma = f_{\alpha}\sigma_{\alpha} + f_{\gamma}\sigma_{\gamma} + f_{m}\sigma_{m} \quad (1)$$

where  $\sigma_{\alpha}$ ,  $\sigma_{\gamma}$ ,  $\sigma_{m}$  are the flow stresses and  $f_{\alpha}$ ,  $f_{\gamma}$ ,  $f_{m}$  are volume fraction of ferrite, austenite and martensite, respectively. It is pertinent to indicate that martensite was obtained during tensile straining because of TRIP effect, and was absent in the original microstructure (Fig. 1). Inserting the fraction of each phase in Eq. (1). The estimates for  $\sigma_{\alpha}$ ,  $\sigma_{\gamma}$ ,  $\sigma_{m}$  are 1045 MPa, 520 MPa and 1990 MPa, respectively. The  $\sigma_{m}$  has a significantly higher value than  $\sigma_{\gamma}$ . Thus, from Eq. (1) and XRD data (Fig. 2c), it is inferred that the sample tempered at lower temperature would have a higher UTS and is related to higher fraction of transformed martensite during tensile test. This further suggests that austenite stability was enhanced with increase in tempering temperature. In the attempt to quantify this behavior, Eq. (2) was used [5,27,28]:

$$f_{\gamma} = f_{\gamma 0} \exp(-k\varepsilon) \quad (2)$$

In Eq. (2),  $f_{\gamma 0}$ ,  $f_{\gamma}$  and  $k$  are the initial austenite fraction, the austenite fraction at strain  $\varepsilon$ , and the mechanical stability of austenite, respectively. A higher value of  $k$  corresponds to a higher driving force for transformation and lower austenite stability. Fig. 4 is a plot of parameter  $k$  with tempering temperature. It is clear that the value of  $k$  decreased with increase in tempering temperature, implying higher austenite stability.

It was previously reported that YS decreased with tempering temperature [29] or was insensitive to tempering temperature [15,30]. To understand the underlying reasons for improvement in YS in the present case (Fig. 3a), two different mechanisms are considered, namely, stress-assisted transformation and strain-induced transformation. The untempered sample with  $\sim$ 80%

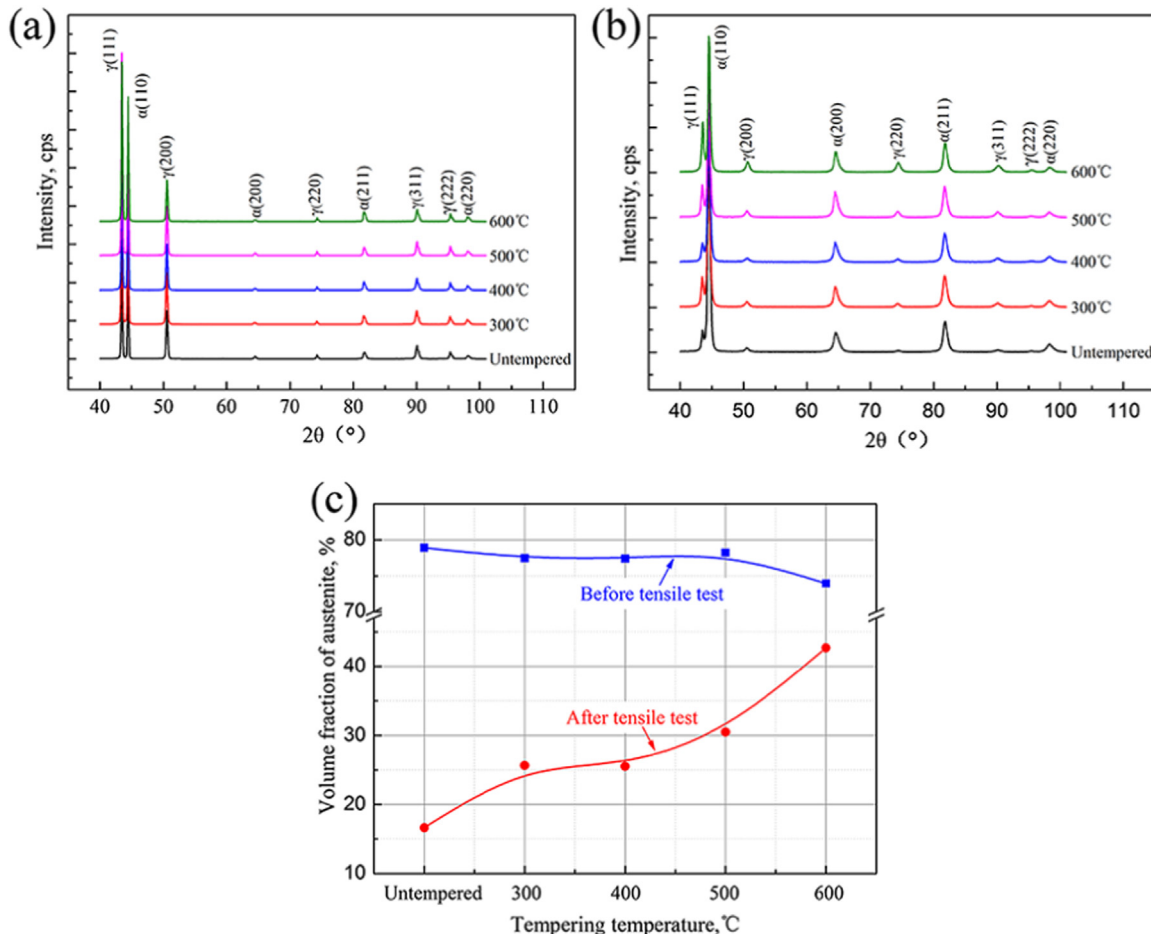


**Fig. 2.** XRD patterns and measured austenite fraction in undeformed and fractured samples tempered at different temperatures. (a) XRD patterns of undeformed samples, (b) XRD patterns of fractured samples, and (c) measured austenite fraction.

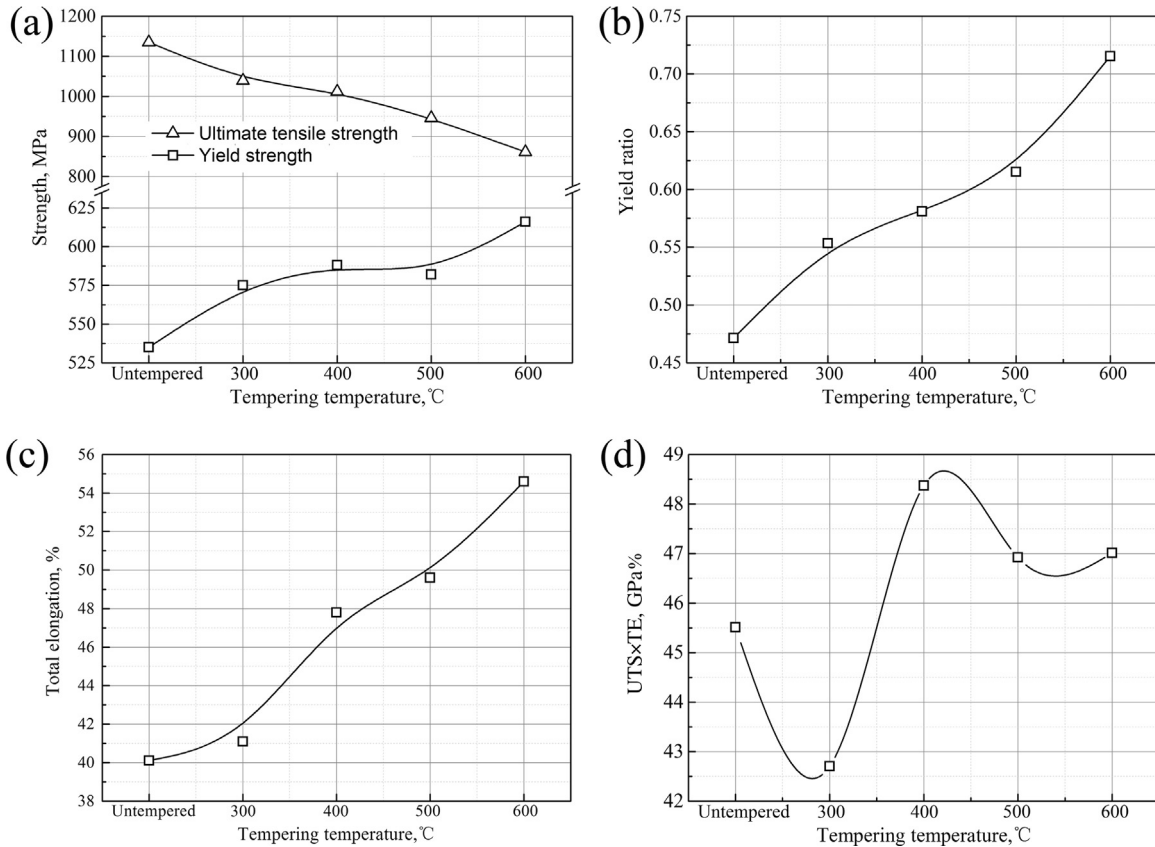


**Fig. 3.** Mechanical properties of tempered samples as a function of tempering temperature. (a) YS and UTS, (b) yield ratio, (c) TE, (d) UTS × TE. (YS: yield strength, UTS: ultimate tensile strength, TE: total elongation).

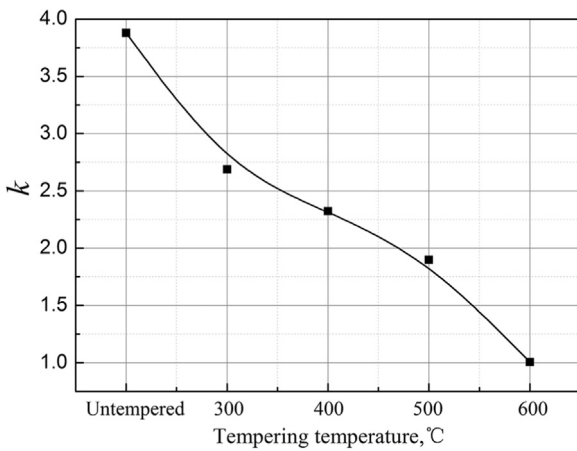


**Fig. 4.** The plots of  $k$  parameter of quenched samples tempered at different temperatures.

austenite is quite similar in behavior to a homogenous austenitic TRIP steel. It is reported in these steels that if the tensile test is performed below the  $M_s^c$  temperature, the martensitic transformation is the dominant deformation mechanism and yielding is not controlled by slip but by martensitic transformation [31,32]. According to the study by Olson and Azrin, for the stress-assisted mechanism, the martensite fraction vs  $\epsilon$  plots are initially linear, while they are sigmoidal when the mechanism is strain-induced transformation [33]. Thus, from Fig. 5, it is inferred that the operating mechanism in the untempered sample is stress-assisted, while the sample tempered at 600 °C (henceforth referred as 600T sample) undergoes strain-induced transformation. Thus, the observed yield strength of 535 MPa for the untempered sample is the

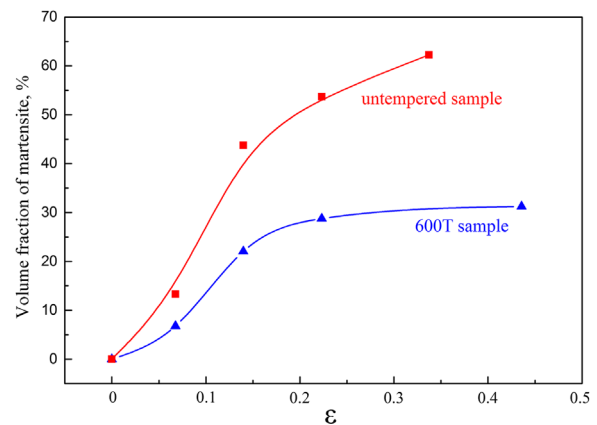


**Fig. 5.** Variation of martensite fraction as a function of true strain for untempered sample and quenched sample tempered at 600 °C (600T sample).

stress required to initiate stress-assisted transformation. With increasing tempering temperature, austenite became more stable (by Mn and C partitioning) and the stress required to initiate the martensitic transformation (yield strength) was increased as indicated in Fig. 3a.

Comparing the austenite content of the undeformed samples with that of the fractured samples (Fig. 2c), it is clear that the TRIP effect waned with increase in tempering temperature. However, the TE increased with tempering temperature. Fig. 6 describes the microstructure of the untempered sample and 600T sample prior to and after tensile straining. On comparing the microstructure of undeformed samples with fractured samples, in the untempered sample, the majority of austenite was transformed into martensite; while in 600T sample, a large fraction of austenite continued

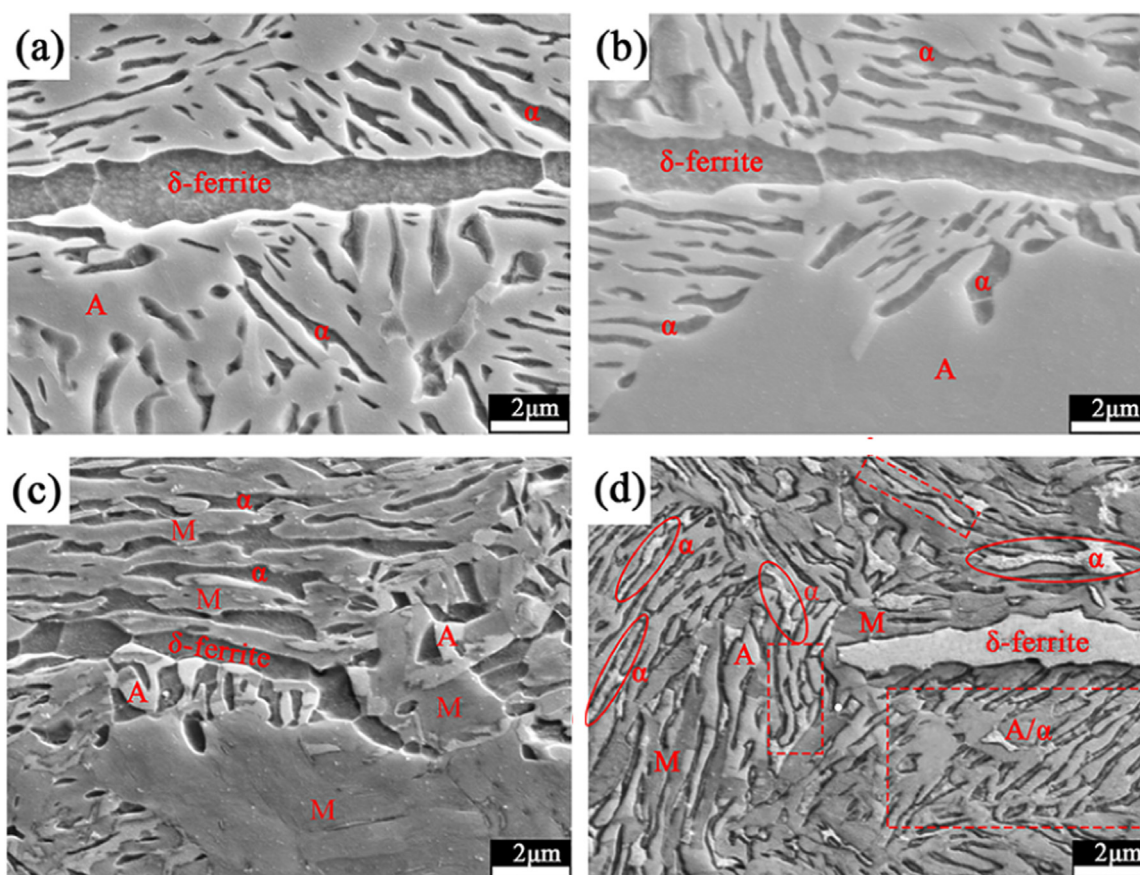


**Fig. 6.** SEM micrographs of (a, c) untempered sample and (b, d) quenched sample tempered at 600 °C prior to and after tensile test. As shown in (c) and (d), martensite was present in the fractured samples. (M: martensite, A: austenite).

to be present, consistent with the XRD data (Fig. 2c). Comparing the microstructure of the two fractured samples, in 600T sample, it was obvious that  $\delta$ -ferrite was considerably squeezed by transformed martensite and deformed austenite during tensile straining. Similarly, it is clear that  $\alpha$ -ferrite (marked with oval circle) was squeezed to fill up the intermediate space and appeared to spill over. A close examination revealed that some austenite grain boundaries (marked with rectangle) were severely deformed. Thus, in 600T sample, significant deformation occurred in austenite,  $\delta$ -ferrite and  $\alpha$ -ferrite occurred during tensile straining. Therefore, the cooperative deformation of austenite,  $\delta$ -ferrite, and  $\alpha$ -ferrite was contributed to the improvement in ductility. In the untempered sample, where majority of austenite transformed to martensite, i.e., TRIP effect contributed to ductility.

### 3.3. Deformation behavior and austenite stability

Work hardening rate (WH) of the untempered sample and the quenched sample tempered at 400, 500, 600 °C (referred as 400T, 500T and 600T sample) are presented in Fig. 7. It is obvious that the samples exhibited three stages of work hardening rate (WH). In all the samples, WH decreased rapidly in stage 1, while it varied with tempering temperature in stage 2. WH of the untempered sample increased at a fast rate, which is similar to other medium-Mn steels [5,34–36]. The work hardening ability begins to weaken with increase in tempering temperature. In the case of 500T sample, WH increased near horizontally, and for 600T sample, it decreased slowly in stage 2. It is obvious that the stage 3 of WH was characterized by serrations, which was attributed to the discontinuous TRIP effect described in our previous study, and it was further revealed that austenite with different stability accounted

for the discontinuous TRIP effect [35,37]. Moreover, the fluctuations in stage 3 diminished with increase in tempering temperature. It is inferred that not only the austenite stability was enhanced, but also the amount of austenite with similar stability was increased. The relationship between work hardening ability and austenite stability can be further elucidated through the interrupted tensile tests.

Fig. 8 shows the variation in volume fraction of austenite as a function of engineering strain measured by XRD for the untempered sample and 600T sample. The volume fraction of austenite decreased with strain in both the samples, but in different manner. The work hardening rate is derived by differentiating Eq. (1) with respect to  $\epsilon$ .

$$\frac{d\sigma}{d\epsilon} = f_{\alpha} \frac{d\sigma_{\alpha}}{d\epsilon} + f_{\gamma} \frac{d\sigma_{\gamma}}{d\epsilon} + f_m \frac{d\sigma_m}{d\epsilon} + \frac{df_m}{d\epsilon} (\sigma_m - \sigma_{\gamma}) \quad (3)$$

For 600T sample, only a small amount of austenite ( $\sim 7\%$ ) transformed into martensite at the engineering strain of 0.07, corresponding to WH of  $\sim 2450$  MPa. In contrast, about 13% of austenite transformed into martensite at similar strain in the untempered sample, corresponding to a WH of  $\sim 2350$  MPa. Though higher fraction of transformed martensite developed in the untempered sample, the WH was lower than the 600T sample. Thus, austenite with low stability transformed at a small strain contributed little to WH.

In stage 1 ( $0 < \epsilon < 0.06$ ), deformation mainly occurred in austenite and ferrite, and the stress produced in the transformed martensite can be regarded as interior stress in austenite. Thus, it is deduced that  $\sigma_m = \sigma_{\gamma}$  and  $d\sigma_m/d\epsilon \approx 0$ . The WH in the initial stage of deformation corresponds to dislocation hardening in

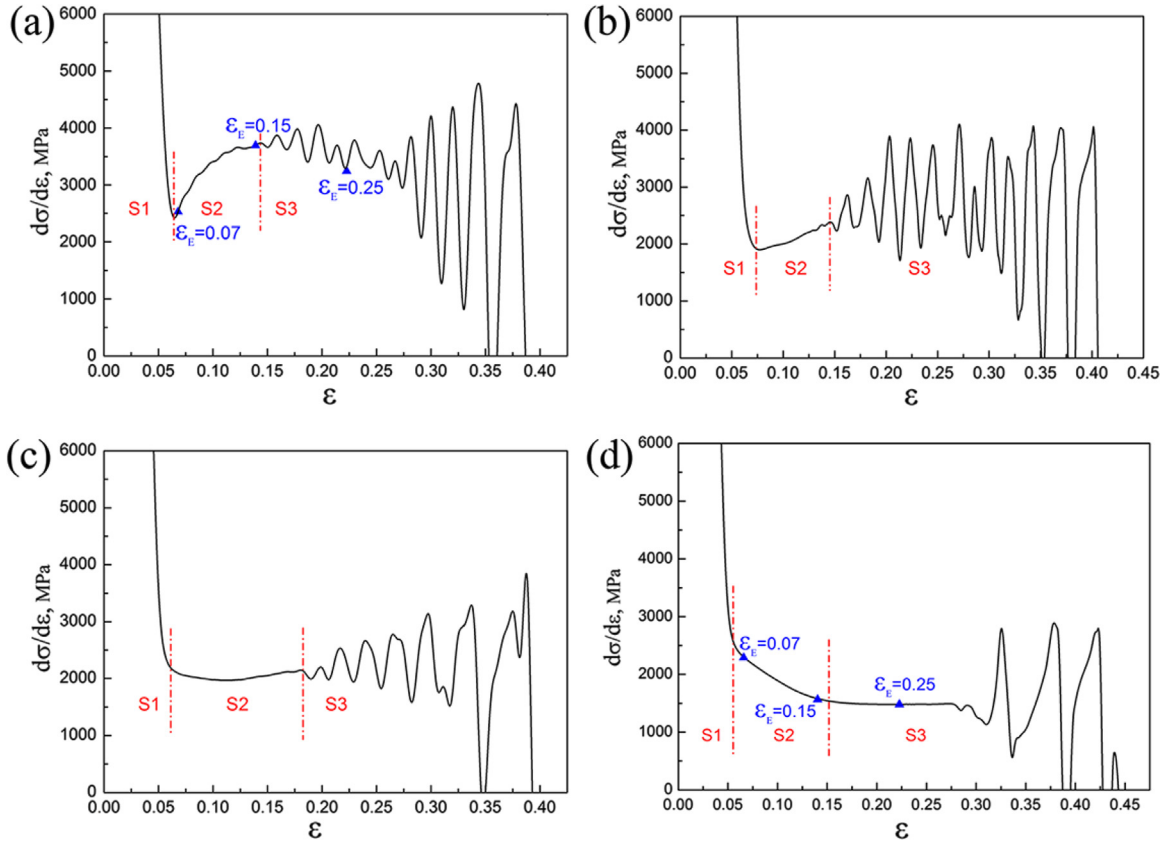


Fig. 7. Work hardening rate of quenched samples tempered at different temperatures. (a) Untempered, (b) 400 °C, (c) 500 °C, and (d) 600 °C.

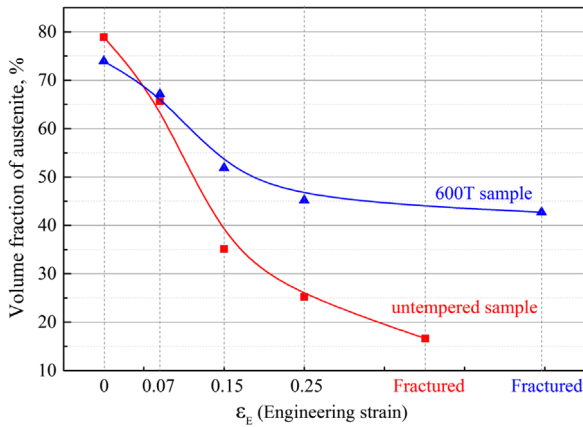


Fig. 8. Variation in austenite fraction in untempered sample and quenched sample tempered at 600 °C (600T sample) subjected to interrupted tensile test.

ferrite and austenite,

$$\frac{d\sigma}{d\varepsilon} \approx f_{\alpha} \frac{d\sigma_{\alpha}}{d\varepsilon} + f_{\gamma} \frac{d\sigma_{\gamma}}{d\varepsilon} \quad (4)$$

The ferrite with higher microhardness than austenite (Table 1), and 600T sample had higher ferrite fraction of 26% than the untempered sample (21%), which are responsible for the higher WH in 600T sample at strain of 0.06.

With increase in strain, the work hardening contribution of austenite and ferrite was decreased after stage 1 and the work hardening contribution of martensite increased with increase in strain. In the untempered sample, in stage 2 ( $0.06 < \varepsilon < 0.14$ ),  $f_m$  increased rapidly (as shown in Fig. 4) with increase in strain, thus,

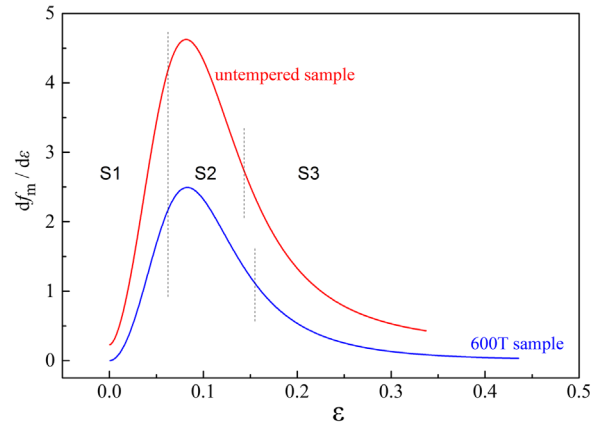
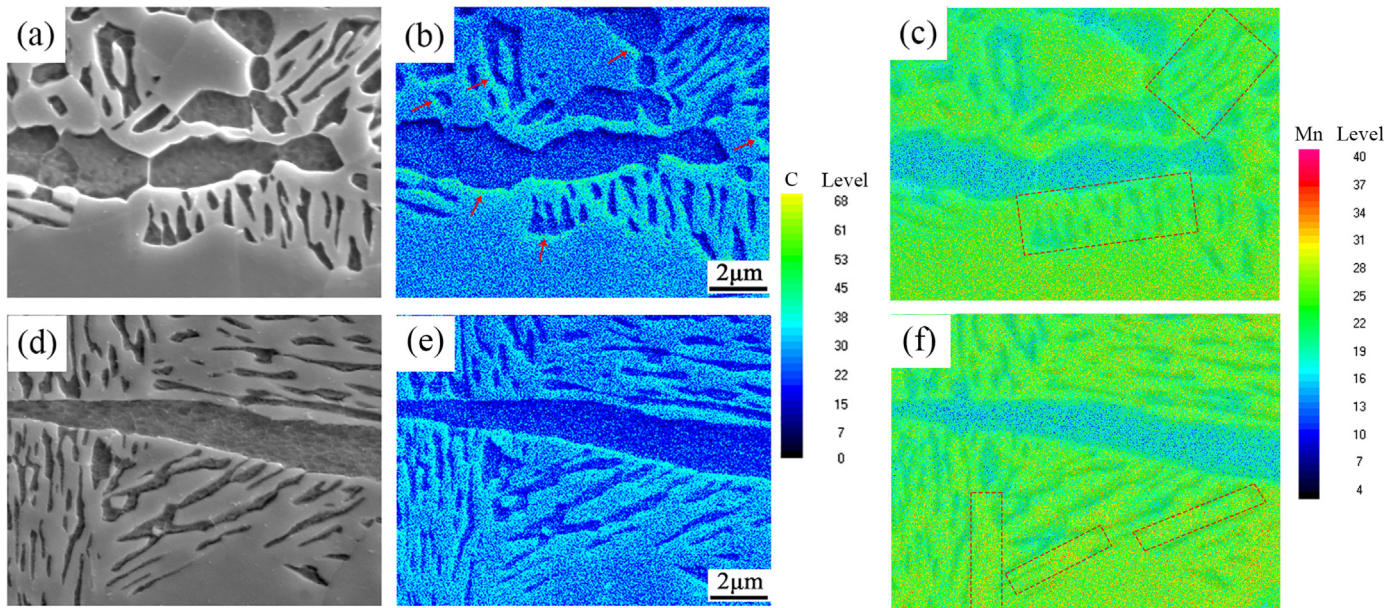


Fig. 9. The differentiation of martensite fraction as a function of true strain.

$$\frac{d\sigma}{d\varepsilon} \approx f_m \frac{d\sigma_m}{d\varepsilon} + \frac{df_m}{d\varepsilon} (\sigma_m - \sigma_{\gamma}) \quad (5)$$

Inserting  $\sigma_{\gamma} = 520$  MPa,  $\sigma_m = 1990$  MPa,  $d\sigma_m/d\varepsilon \approx 0$  and  $df_m/d\varepsilon = 2.7$  (Fig. 9) at strain of 0.14, the calculated WH was 3969 MPa, which agrees well with the WH of 3780 MPa in Fig. 7a. In 600T sample, in stage 2 ( $0.06 < \varepsilon < 0.15$ ),  $f_m$  increases gently with increase in strain, and the corresponding value of  $df_m/d\varepsilon$  was 1.1 at strain of 0.15. Thus, the WH could be estimated in a similar manner was 1617 MPa, which agrees well with the WH of 1554 MPa in Fig. 7d.

Based on our recent studies [35,37], the fluctuation in stage 3 resulted from discontinuous TRIP effect because of the presence of austenite with different degree of stability. As the fluctuations decreased with increase in tempering temperature (Fig. 7), the



**Fig. 10.** SEM micrographs of (a) untempered sample and (d) quenched sample tempered at 600 °C. (b, c) and (e, f) are corresponding carbon and manganese concentration by EPMA.

amount of austenite with similar stability was increased. On the basis of the aforementioned discussion, the diffusion of alloying elements accounts for the observed behavior. The concentration of C and Mn was more uniform in austenite, and is attributed to adequate diffusion of C and Mn with increase in tempering temperature, and was further confirmed by EMPA.

Fig. 10 shows the distribution of C and Mn concentration in the untempered sample and 600T sample. In the untempered sample, it was obvious that the lath-type austenite had higher carbon concentration but lower Mn content than the adjacent blocky austenite (Fig. 10b and c). Moreover, carbon was found to be enriched at the grain boundaries (as marked by arrows in Fig. 10b). In 600T sample, it was clear that the distribution of carbon was more uniform than the untempered sample. Furthermore, the lath-type austenite had Mn-concentration similar to the adjacent blocky austenite, as marked with rectangle in Fig. 10f. Comparing Fig. 10c with f, we can deduce that Mn diffused from the blocky austenite to the lath-type austenite during tempering. Consequently, it was inferred that the diffusion of Mn and C was greater in austenite and ferrite grains with increase in tempering temperature, which enhanced the stability of austenite. In the attempt to clarify the partitioning behavior of Mn and C during intercritical annealing and tempering on austenite stability, simulations using DICTRA software were conducted.

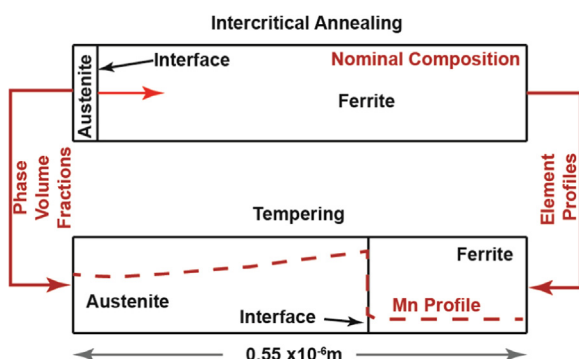


**Fig. 11.** Initial conditions implemented in DICTRA. The results from intercritical annealing model were used as input in the tempering model.

### 3.4. Simulation

A single cell planar geometry was employed, as shown in Fig. 11, with domain size equal to 0.55  $\mu\text{m}$  corresponding to one-half the measured ferrite-to-austenite mean distance (center to center), as depicted in the micrograph of Fig. 1a. To simulate intercritical annealing, a thin austenite region, 50 nm size, was attached to the left of the ferrite region. The two regions were discretized with a linear grid possessing a higher density of grid points at the interface. The initial composition of the austenite slice and ferrite regions was considered equal to the nominal alloy composition. Identical single cell geometry was used for the simulation of tempering, however with different initial conditions. The volume fraction of austenite and the composition of austenite and ferrite correspond to the results of the intercritical annealing simulation at 775 °C for 3600 s. In other words, the results of intercritical annealing simulation were used as initial conditions for tempering simulation. Zero flux boundary conditions (closed system) were considered as the upper and lower boundaries of the system. Throughout the simulation local equilibrium (LE) conditions were imposed. Given that TEM indicated that austenite before tempering exhibited a high dislocation density, thus, in the case of calculations for tempered samples, the dislocation density effect on the diffusion coefficient was taken into consideration. In DICTRA, this is possible by (a) modifying the bulk mobility with a reduction in activation energy to 80% the value for bulk diffusion and (b) by taking into account a contribution proportional to  $\rho b^2$ , where  $\rho$  is the dislocation density and  $b$  the Burgers vector. A value of  $\rho = 10^9 \text{ mm}^{-2}$  was adopted in this work.

Solute partitioning after intercritical annealing and followed by tempering at 600 °C are depicted in Fig. 12a for manganese and Fig. 12b for carbon, respectively. After intercritical annealing there was a slight enrichment of austenite in both manganese and carbon, while the interface position corresponds to 0.79 austenite volume fraction, which compared well with the measured volume fraction of 0.79 from the XRD data of Fig. 2c for the untempered condition. Two effects were observed after tempering at 600 °C. The first is a short retraction of the interface, corresponding to the reduction of the austenite fraction to 0.74, which also compared well with the measured fraction of 0.74 from the XRD data

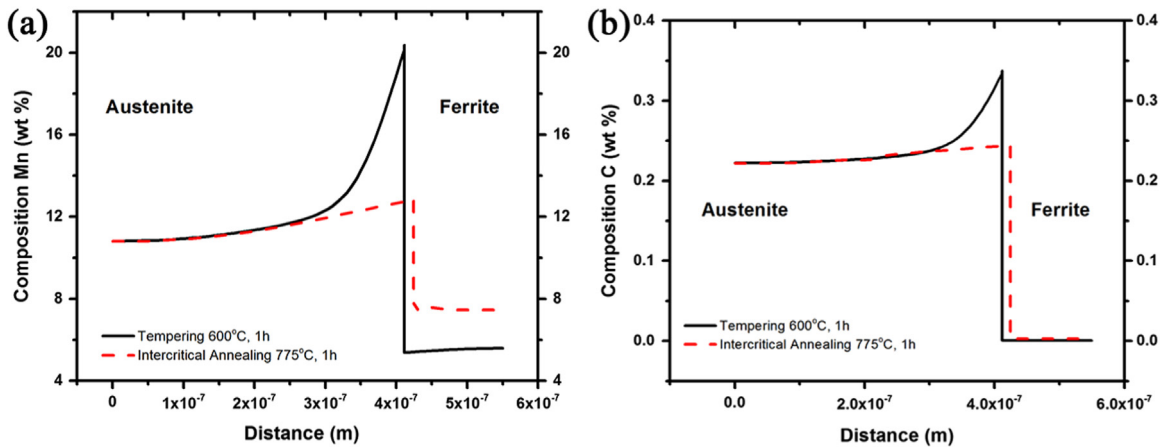


**Fig. 12.** Profile of (a) Mn and (b) carbon after intercritical annealing at 775 °C for 1 h (red dotted line) and tempering at 600 °C for 1 h (black line). (For interpretation of the references to color in this figure legend, the reader is referred to the web version of this article.)

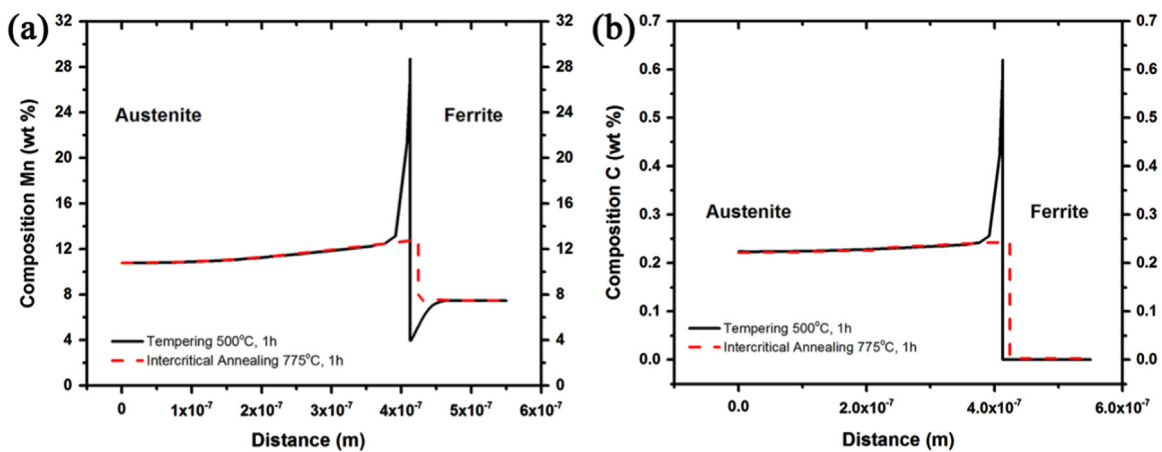


**Fig. 13.** Profile of (a) Mn and (b) carbon after intercritical annealing at 775 °C for 1 h (red dotted line) and tempering at 500 °C for 1 h (black line). (For interpretation of the references to color in this figure legend, the reader is referred to the web version of this article.)

(Fig. 2c). The second effect is further enrichment of austenite in both manganese and carbon for at least half the grain diameter, while in the rest of the grain the composition profile did not appreciably change relative to intercritical annealing. This substantial enrichment can explain the enhanced stability of austenite depicted in Fig. 8. Corresponding results for tempering at 500 °C are shown in Fig. 13a for manganese and Fig. 13b for carbon. The austenite fraction was reduced after tempering to 0.75, which is consistent with the measured fraction of 0.78 from the XRD data (Fig. 2c). The manganese and carbon enrichment was not extended to the level as in 600 °C tempering and was more confined to austenite/ferrite interface. This led to lower austenite stability relative to 600 °C tempering, in agreement with the data of Fig. 2c. Combining Figs. 12 and 13, it is inferred that due to enhanced diffusing ability, the distribution of Mn and C in austenite becomes uniform with increase in tempering temperature, which are in qualitative agreement with the EPMA results of Fig. 10, leading to decrease in fluctuations in stage 3 of WH (Fig. 7).

#### 4. Conclusions

The effect of intercritical annealing and tempering temperature on the mechanical properties and deformation behavior of hot rolled Fe–0.18C–10.62Mn–4.06Al–0.03Nb TRIP steel was studied. The conclusions are as follows.

- (1) The ultimate tensile strength decreased with increase in tempering temperature and was associated with waning TRIP effect. However, the total elongation increased with increase in tempering temperature, and was attributed to the enhanced contribution from the cooperative deformation of austenite,  $\delta$ -ferrite, and  $\alpha$ -ferrite during tensile straining.
- (2) The martensite transformation mechanisms (stress-assisted or strain-induced) accounted for the variation in yield strength. The untempered sample was characterized by stress-assisted transformation, and the observed yield strength of 535 MPa is the stress required to initiate stress-assisted transformation. With increasing tempering temperature, austenite became more stable and the stress required to initiate the martensitic transformation (yield strength) was increased. For 600T sample, the transformation was strain-induced.
- (3) The observed three-stage work hardening behavior was explained via the dynamic composite nature of the steel. The deformation of ferrite and austenite governed stage 1, and austenite with low stability that transformed in the initial stage had little contribution to WH. The enhanced WH in stage 2 was related to continuously transformed martensite. Moreover, the distribution of Mn and C in austenite became uniform, leading to decrease in fluctuations in stage 3 of WH.
- (4) Tempering temperature had little effect on austenite fraction, but it significantly increased the austenite stability with increase in tempering temperature, which mainly resulted from the enhanced diffusion of Mn and C to the austenite grains and

austenite/ferrite grains. The theoretical simulation on partitioning of alloying elements was consistent with the experimental results.

## Acknowledgments

The present study was financially supported by the National Natural Foundation for Young Scientists of China (No. 51501035) and Chinese Postdoctoral Science Foundation (2015M580230). RDKM gratefully acknowledges support from University of Texas at El Paso, USA and by the National Science Foundation through grant number DMR 1458074.

## References

- [1] B.C. De Cooman, *Curr. Opin. St. M.* 8 (2004) 285–303.
- [2] T. Heller, A. Nuss, in: M. Militzer, W.J. Poole, E. Essadiqi (Eds.), *Proceedings of the International Symposium on Transformation and Deformation Mechanisms in Advanced High Strength Steels*, CIM, Montreal, 2003, pp. 7–20.
- [3] L. Samek, E. De Moor, J. Penning, B.C. De Cooman, *Metall. Mater. Trans.* 37 (2006) 109–124.
- [4] S. Lee, S.-J. Lee, B.C. De Cooman, *Scr. Mater.* 65 (2011) 225–228.
- [5] J. Shi, X.J. Sun, M.Q. Wang, W.J. Hui, H. Dong, W.Q. Cao, *Scr. Mater.* 63 (2010) 815–818.
- [6] M.J. Merwin, *Mater. Sci. Forum.* 539–543 (2007) 4327–4332.
- [7] S. Lee, S.-J. Lee, S.S. Kumar, K. Lee, B.C. De Cooman, *Metall. Mater. Trans. A* 42A (2011) 3638–3651.
- [8] P.J. Gibbs, E. De Moor, M.J. Merwin, B. Clausen, J.G. Speer, D.K. Matlock, *Metall. Mater. Trans. A* 42A (2011) 3691–3702.
- [9] J. Shi, W.Q. Cao, H. Dong, *Mater. Sci. Forum.* 654–656 (2010) 238–241.
- [10] C. Wang, J. Shi, C.Y. Wang, W.J. Hui, M.Q. Wang, H. Dong, W.Q. Cao, *ISIJ Int.* 51 (2011) 651–656.
- [11] W.Q. Cao, C. Wang, J. Shi, M.Q. Wang, W.J. Hui, H. Dong, *Mater. Sci. Eng. A* 528 (2011) 6661–6666.
- [12] Z.H. Cai, H. Ding, X. Xue, Q.B. Xin, *Mater. Sci. Eng. A* 560 (2013) 388–395.
- [13] Z.H. Cai, H. Ding, X. Xue, R.D.K. Misra, H. Kong, H.Y. Wu, *Mater. Sci. Eng. A* 595 (2014) 86–91.
- [14] Y. Luo, J.M. Peng, H.B. Wang, X.C. Wu, *Mater. Sci. Eng. A* 527 (2010) 3433–3437.
- [15] M.W. Tong, P.K.C. Venkatsurya, W.H. Zhou, R.D.K. Misra, B. Guo, K.G. Zhang, W. Fan, *Mater. Sci. Eng. A* 609 (2014) 209–216.
- [16] H.F. Xu, J. Zhao, W.Q. Cao, J. Shi, C.Y. Wang, J. Li, H. Dong, *ISIJ Int.* 52 (2012) 868–873.
- [17] G. Thomas, *Metal. Trans. A* 9A (1978) 439–450.
- [18] T. Bhattacharyya, S.B. Singh, S. Das, A. Haldar, D. Bhattacharjee, *Mater. Sci. Eng. A* 528 (2011) 2394–2400.
- [19] G.N. Haidemenopoulos, A.I. katsamas, N. Aravas, *Steel Res. Int.* 77 (2006) 720–726.
- [20] G.N. Haidemenopoulos, A.N. Vasilakos, *J. Alloy. Compd.* 247 (1997) 128–133.
- [21] B.K. Jha, R. Avtar, V. Sagar Dwivedi, *Trans. Indian Inst. Met.* 49 (1996) 133–142.
- [22] J.O. Andersson, T. Helander, L. Höglund, B. Sundman, *Calphad* 26 (2002) 273–312.
- [23] D. Embury, O. Bouaziz, *Annu. Rev. Mater. Res.* 40 (2010) 243–270.
- [24] S.H. Li, W.J. Dan, W.G. Zhang, Z.Q. Lin, *Comp. Mater. Sci.* 40 (2007) 292–299.
- [25] S. Lee, B.C. De Cooman, *Met. Mater. Trans. A* 45A (2014) 6039–6052.
- [26] Z.C. Li, H. Ding, Z.H. Cai, *Mater. Sci. Eng. A* 639 (2015) 559–566.
- [27] S. Zhang, K.O. Findley, *Acta Mater.* 61 (2013) 1895–1903.
- [28] S. Zhou, K. Zhang, Y. Wang, J.F. Gu, Y.H. Rong, *Mater. Sci. Eng. A* 528 (2011) 8006–8012.
- [29] B. Qin, Z.Y. Wang, Q.S. Sun, *Mater. Charact.* 59 (2008) 1096–1100.
- [30] W.H. Zhou, V.S.A. Challa, H. Guo, C.J. Shang, R.D.K. Misra, *Mater. Sci. Eng. A* 620 (2015) 454–462.
- [31] G.B. Olson, M. Cohen, *J. Less-Common Met.* 28 (1972) 107–118.
- [32] G.B. Olson, M. Cohen, *Met. Trans. A* 6A (1975) 791–795.
- [33] G.B. Olson, M. Azrin, *Metall. Trans. A* 9A (1978) 713–721.
- [34] Z.H. Cai, H. Ding, X. Xue, J. Jiang, Q.B. Xin, R.D.K. Misra, *Scr. Mater.* 68 (2013) 865–868.
- [35] Z.H. Cai, H. Ding, R.D.K. Misra, H. Kong, *Scr. Mater.* 71 (2014) 5–8.
- [36] W.J. Dan, S.H. Li, W.G. Zhang, Z.Q. Lin, *Mater. Des.* 29 (2008) 604–612.
- [37] Z.H. Cai, H. Ding, R.D.K. Misra, Z.Y. Ying, *Acta Mater.* 84 (2015) 229–236.